A Test Case of Correlation Metric Construction of a Reaction Pathway from Measurements

Adam Arkin, Peidong Shen, John Ross*

A method for the prediction of the interactions within complex reaction networks from experimentally measured time series of the concentration of the species composing the system has been tested experimentally on the first few steps of the glycolytic pathway. The reconstituted reaction system, containing eight enzymes and 14 metabolic intermediates, was kept away from equilibrium in a continuous-flow, stirred-tank reactor. Input concentrations of adenosine monophosphate and citrate were externally varied over time, and their concentrations in the reactor and the response of eight other species were measured. Multidimensional scaling analysis and heuristic algorithms applied to two-species time-lagged correlation functions derived from the time series yielded a diagram from which the interactions among all of the species could be deduced. The diagram predicts essential features of the known reaction network in regard to chemical reactions and interactions among the measured species. The approach is applicable to many complex reaction systems.

Traditionally, chemical kinetics reveals the mechanism of a chemical reaction by establishing the sequence and rates of individual elementary steps. In multistep chemical reactions, such as combustion or metabolic pathways, complex networks of reactants and products may be set up that involve numerous elementary steps and multiple feedbacks whose significance varies at different overall concentrations. Thus, the reductionist approach of identifying and isolating individual reaction steps can be experimentally daunting in that it requires purifying the individual components and finding all of the interactions that constitute the complete mechanism. These problems are especially prevalent in enzymatic and genetic reaction systems in which the catalyst for a single reaction can have tens of interacting effectors.

We recently presented a method, called correlation metric construction (CMC) (*1*), that takes a different approach to the analysis of complex chemical kinetics. A chemical reaction system operating near a steady state (but far from equilibrium) is subjected to random perturbations in the concentrations of a set of input species. Given that we can measure chemical concentrations of species in situ, we analyze the response of these concentrations to the input variation. From these time series data, the method is used to deduce the reaction pathway underlying the response dynamics. It has been tested successfully on several numerical model reaction systems, but several issues need to be addressed to prove experimental feasibility. These issues include the determination of (i) the number of data points and time resolution necessary for analysis, both in regard to the number of time points per chemical concentration series and the number of chemical species that can be measured simultaneously, (ii) the effects of measurement error, and (iii) the presence of unmeasured species.

Although it is possible to address the issues theoretically, the most convincing argument for feasibility is substantiation by experiment. We present an analysis of data for an enzymatic reaction network, the initial steps of glycolysis (Fig. 1). Glycolysis is central in intermediary metabolism and has a high degree of regulation (*2*). The reaction pathway has been well studied and thus is a good test for the theory. Further, the reaction mechanism of this part of glycolysis has been modeled extensively (*3*).

The quantity and precision of the measurements reported here are sufficient to determine the matrix of correlation functions and, from this, a reaction pathway that is qualitatively consistent with the reaction mechanism established previously. The existence of unmeasured species did not compromise the analysis. The quantity and precision of the data were not excessive, and thus, we expect the method to be generally applicable.

This CMC experiment was carried out in a continuous-flow, stirred-tank reactor (CSTR). The reaction network considered consists of eight enzymes, which catalyze the conversion of glucose into dihydroxyacetone phosphate and glyceraldehyde phosphate. Enzymes were confined to the reactor by an ultrafiltration membrane at the top of the reactor (*4*). The membrane was permeable to all low–molecular weight species (*5*).

The inputs are (i) a reaction buffer, which provides starting material for the reaction network to process, maintains pH and pMg, and contains any other species that act as constant constraints on the system dynamics, and (ii) a set of "control species" (at least one), whose input concentrations are changed randomly every sampling period over the course of the experiment. The sampling period is chosen such that the system almost, but not quite, relaxes to its nonequilibrium steady state. The system is kept near enough to its steady state to minimize trending (caused by the relaxation) in the time series, but far enough from the steady state that the time-lagged autocorrelation functions for each species decays to zero over three to five sampling periods. This long decay is necessary if temporal ordering in the network is to be analyzed.

We used capillary zone electrophoresis (CZE) (*6*) to measure accurately the concentrations of most of the small molecular species that are passed through the mem-

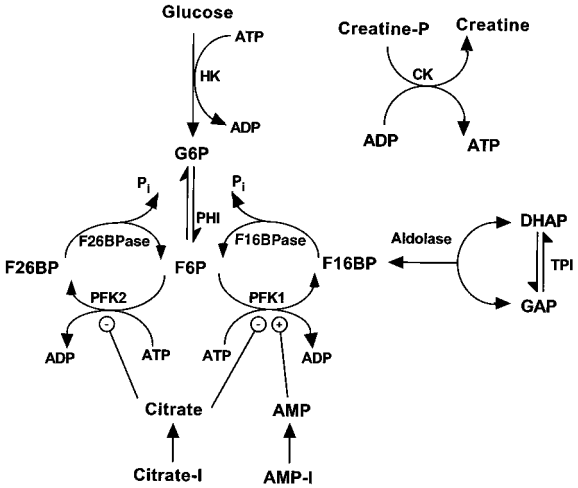

Fig. 1. The first few reaction steps of glycolysis (*7*). Lines ending in circles denote regulatory interaction; minus signs indicate a negative effector; plus signs, a positive effector. Creatine-P and CK keep the concentrations of ATP and ADP constant.

Department of Chemistry, Stanford University, Stanford, CA 94305, USA.

*To whom correspondence should be addressed.

brane. Because the enzymes are not present, the concentrations in aliquots taken from the reactor outflow just before the end of each sampling period reflect the concentrations inside the reactor. The set of perturbing input species concentrations and system responses form an ordered time series suitable for analysis by CMC.

We measured the concentrations of P_i, G6P, F6P, F16BP, F26BP, and DHAP, as well as the input and reactor concentrations of citrate and AMP (*7*). We developed a CZE detection method specifically for the separation and quantification of the metabolites in glycolysis (*8*). Using 5.5 mM 4-hydroxybenzoate (pH 11.8) as background electrolyte and indirect ultraviolet detection, we analyzed simultaneously the components mentioned above and several others in an enzyme buffer (*9, 10*). The analysis of a single sample took less than 6 min to complete. The detection limit for each species was defined as a signal-to-noise ratio of 3:1 and was determined to be 0.003 mM for P_i, 0.001 mM for F16BP and F26BP, and 0.002 mM for G6P, F6P, DHAP, citrate, and AMP. The error in repeated measurements of standard concentrations of these species was 2% for P_i, 1% for F16BP, 7% for F26BP, 2% for G6P, 3% for F6P, 1% for DHAP, 2% for citrate, and 3% for AMP.

To begin a CMC experiment, the CSTR was primed by flowing in the glycolytic enzymes to the following total activities: 4.0 units of HK, 10 units of PHI, 0.96 units of PFK1, 0.25 units of F16BPase, 0.01 units of PFK2::F26BPase, 0.86 units of aldolase, 10 units of TPI, and 75 units of CK (*9*). These activities were chosen to yield physiologically relevant concentrations of the intermediates, with the exception of F26BP, the concentration of which was set high enough to be measurable by our CZE method.

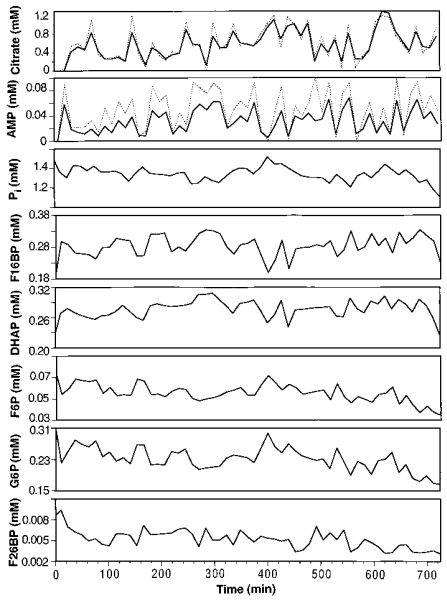

Fig. 2. The time courses of measured concentration of the inputs, AMP and citrate, in the experiments, with the responses of the concentrations of P_i and of the species F16BP, DHAP, F6P, G6P, and F26BP. The dotted curves are the known input concentrations for AMP and citrate.

The input flow into the reactor (held constant at 0.2 ml/min) contained enzyme buffer (*9*), which includes, among other things, 0.6 mM glucose and 2.5 mM creatine-P. Glucose is the feed-reactant from which the process of glycolysis is initiated. The combination of CK and creatine-P was included to fix the ATP:ADP ratio during the course of the experiment. The reactor steady state reached when the inflow contains only these species is defined as the reference state; the intermediate concentrations were 1.48 mM P_i, 0.0086 mM F26BP, 0.20 mM F16BP, 0.072 mM F6P, 0.31 mM G6P, and 0.23 mM DHAP.

As input species, we chose two well-known indicators of cell nutrition level, AMP and citrate. AMP is an activator of PFK1 and promotes glycolysis (*11, 12*), whereas citrate is an inhibitor of both PFK1 and PFK2 and inhibits glycolysis (*11, 13, 14*). Two 55-point, uniformly random, uncorrelated time series of concentration were generated by computer: one series for AMP over the range 0 to 0.1 mM, and one for citrate over the range 0 to 1.2 mM. These ranges represent the extreme "physiological" concentrations attained by these species.

At the start of the experiment, the system was placed in the reference state. While conserving the volume of the inflow, we then flowed the first set of input concentrations into the reactor. For each set of inputs in the time series, the system was allowed to relax for 10 min, and an aliquot (0.1 ml) was collected from the outflow. Hydrolysis of the sugars, including F26BP, was minimal as long as the samples were either immediately analyzed or kept frozen. The system was allowed to relax for an additional 3 min before the input concentrations were changed and the process repeated (Fig. 2). This 13-min sampling period was chosen to be much longer than the residence time of the reactor (~6 min) but, as determined empirically, not enough time for the system to relax completely to steady state after an average perturbation (*15*).

The measurements were analyzed according to the theory presented in (*1*). Briefly, the time-lagged correlation matrix $\mathbf{R}(\tau) = [r_{ij}(\tau)]$ is first calculated with the equations

$$S_{ij}(\tau) = \langle [x_i(t) - \bar{x}_i][x_j(t + \tau) - \bar{x}_j] \rangle \quad (1)$$

$$r_{ij}(\tau) = \frac{S_{ij}(\tau)}{\sqrt{S_{ii}(\tau)S_{jj}(\tau)}} \quad (2)$$

here the angle brackets denote a time average over all of the measurements, $x_i(t)$ is the tth time point of the time series generated for species i, and $\bar{x}_i$ is the time average of the ith time series. The indices i and j range over all species. Other methods of kinetic analysis have also used a correlation measure of relatedness between species (*16*). Next, $\mathbf{R}(\tau)$ is converted into a Euclidean distance matrix with the canonical transformation

$$d_{ij} = (c_{ii} - 2c_{ij} + c_{jj})^{1/2} = \sqrt{2}(1.0 - c_{ij})^{1/2} \quad (3)$$

$$c_{ij} = \max |r_{ij}(\tau)|_\tau \quad (4)$$

where Eq. 4 defines c_{ij} to be the absolute value of the maximum correlation between the time series for species i and that for species j, regardless of the value of τ. We define $\mathbf{D} = (d_{ij})$ to be the distance matrix. Finally, a classical multidimensional scaling (MDS) method is applied to $\mathbf{D}$ to find a consistent configuration of points representing each of the species as well as the dimension Δ of the system. This calculation is accomplished by finding the eigenvalues λ_i and eigenvectors $\mathbf{z}_i$ of the centered inner product matrix $\mathbf{B}$ defined by

$$\mathbf{B} = -\frac{1}{2}\mathbf{H}(d_{ij}^2)\mathbf{H} \quad (5)$$

$$\mathbf{H} = \mathbf{I} - \frac{1}{M}\mathbf{1}\mathbf{1}' \quad (6)$$

where $\mathbf{H}$ is the centering matrix, $\mathbf{I}$ is the $M \times M$ identity matrix, and $\mathbf{1}\mathbf{1}'$ is the $M \times M$ unit matrix. Each eigenvector of $\mathbf{B}$ corresponds to a principal coordinate axis for the points implied by the distance matrix. The eigenvectors are normalized such that $\mathbf{z}_i\mathbf{z}_i = \lambda_i$. A point represents a particular time series generated for a given chemical species. The eigenvalue for an eigenvector is a measure of the amount of the total object (the set of all of the points) projected onto the particular eigenvector. The dimension of the system Δ is defined to be the minimal number of eigenvectors such that greater than 99% of the object is projected onto those eigenvectors. For graphical purposes, it is often most useful to plot the projection of the object on the first two (largest eigenvalue) principal axes so that the configuration of points is easy to visualize. The analysis outlined here is merely the simplest; many improvements are possible.

A representative three-dimensional (3D) section of the entire correlation function calculated from Eq. 2 is shown in Fig. 3A. This section shows the lagged correlations of the time series of all species in the system with G6P. It shows strong positive and negative dependencies of G6P varia-

tion on a number of other species and the inputs. The smooth decline, with increasing absolute lag, of the autocorrelation of G6P from its maximum at $\tau = 0$ implies that the system is not completely at steady state. Thus, some temporal ordering of variation in each of the variables may be assigned (Fig. 3B). If the time series for a given species has a maximum correlation at negative lags compared to a reference time series, then that species receives the input signals after the reference series, and vice versa. Similarly, if the two series are maximally correlated at zero lag but correlation tails to negative (positive) lags, variation in the given species closely follows (precedes) variation in the reference species. For example, the tailing to positive lags of the correlation of G6P with AMP-I implies that variations in AMP-I precede variation in G6P, that is, variations in G6P are responses to variations in AMP.

A graphical matrix summary of the distance, connection, and temporal data derived from the correlation functions is shown in Fig. 4. A network hypothesis for the system is derived simply by drawing arrows, in the directions indicated by the + and − symbols, between all connected species. The matrix also gives a rough idea of how "central" each species is to the dynamics of the network. For example, as indicated by the number of dark matrix elements in their rows and columns, AMP is a much stronger effector of network dynamics than is citrate.

The annotated MDS diagram is automatically constructed from the data graphically displayed in Fig. 4. The diagram summarizes the strength of interaction and predicts mechanistic connections between species. To derive the positions of the species on the diagram, one performs MDS on the distance matrix. The distance between points on the diagram represents the strength of correlation between the two species. About 85% of the MDS object is contained in two dimensions. The 2D projection of the object (Fig. 5A) is thus a fairly good representation of the correlation distances among all the species in the network.

We can analyze the MDS diagram in Fig. 5A as if we had no knowledge of the glycolytic pathway and then compare the results to the known network. First, as expected, the measured concentrations of AMP and citrate in the reactor are tightly correlated to their own input concentrations (AMP-I and citrate-I; see Fig. 2), and variation in the concentrations of these species is preceded by variation in their inputs (Fig. 4). Citrate evidently strongly affects the concentration of F26BP: Variation in citrate precedes variation in F26BP, and increase of citrate in the system leads to decrease of F26BP. Citrate is positively correlated with F6P and is unlikely to react directly with F26BP; it is therefore predicted that citrate either inhibits the conversion of F6P to F26BP or activates the reverse reaction, or both.

The species F6P and G6P are almost too tightly correlated to be distinguished. Given their strong correlation, and because F6P is a simple isomer of G6P, they probably interconvert. The positive correlation between them implies that when material flows into either species, it is quickly repartitioned between them. Therefore, they are likely connected by a quasi-equilibrium reaction. According to temporal ordering, however, fluctuation in F6P closely precedes response in G6P, and thus, G6P is mechanistically further from the input species than F6P; that is, variation in the inputs must travel through more reaction steps to get to G6P than to get to F6P. Thus, although G6P is connected to AMP by the connection algorithm, temporal ordering, the strength of the correlation be-

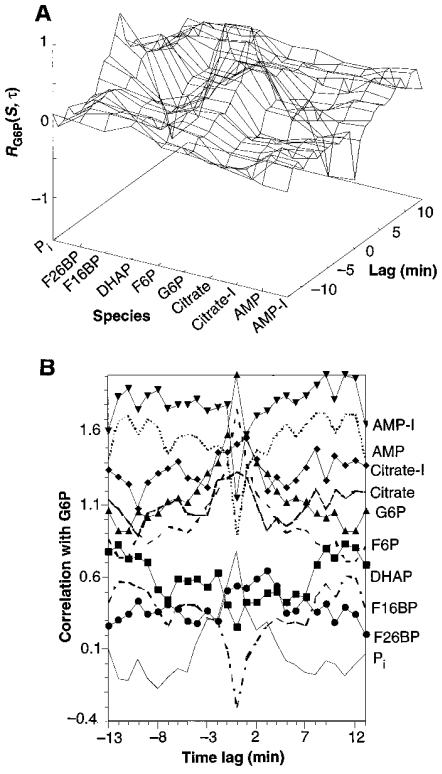

Fig. 3. (**A**) Plot of the time-lagged correlation function R of G6P with all other species. Each lag represents a time of 13 min. (**B**) Graphs of the lagged correlation functions in (A) offset to distinguish individual correlation functions. Each successive correlation function, starting with F26BP, is offset by 0.2 unit on the correlation axis. The graph clarifies the temporal ordering data inherent in the correlation functions. For example, the maximum correlation with F26BP occurs at significantly positive lags, implying that variation in F26BP precedes variation in G6P.

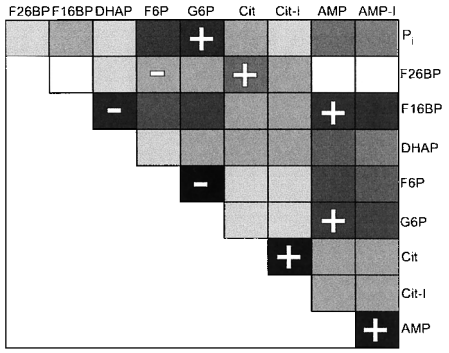

Fig. 4. Matrix summary of distance matrix, connection algorithm, and temporal ordering algorithm. The shade of each matrix element represents the distance between two species, calculated from the correlation function matrix by means of Eqs. 3 and 4. The darker the shade, the smaller the distance (white $\rightarrow d_{ij} = 1.3$, black $\rightarrow d_{ij} = 0.2$; linear gray scale). A + or − within a matrix element denotes that the connection algorithm has assigned a significant connection between these two species: a + (−) indicates that response of the row species follows (precedes) variation in the column species.

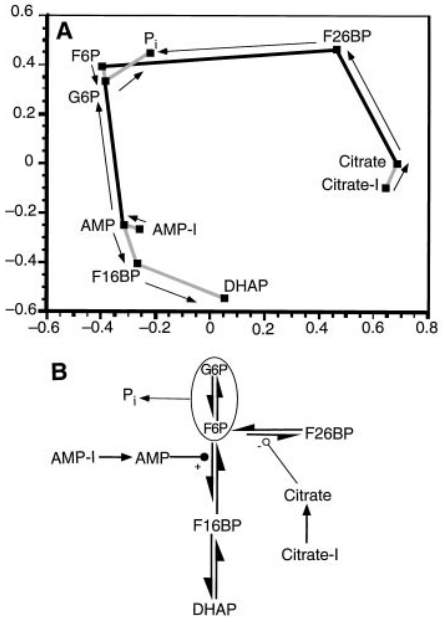

Fig. 5. (**A**) The 2D projection of the MDS diagram for the time series shown in Fig. 2. Each point represents the time series of a given species. The closer two points are, the higher the correlation between the respective time series. Lines were drawn with the connection algorithm described in (*1*). Black (gray) lines indicate negative (positive) correlation between the respective species. Arrows indicate temporal ordering among species based on the lagged correlations between the their time series. (**B**) The predicted reaction pathway derived from the CMC diagram. Its correspondence to the known mechanism (Fig. 1) is high.

tween G6P and F6P, and the chemical argument below imply that that connection from AMP may be to F6P.

The F6P/G6P cluster has a positive correlation with P_i and negative correlations with F26BP and AMP. This relation implies that F6P and G6P are either converted to these species or are involved in reactions controlled by them. Thus, because it is easy to imagine that F6P is converted to F26BP (and back again), and because phosphate is produced when F6P/G6P is produced, the prediction that F6P is interconverted with F26BP is supported. The time ordering of the F26BP-F6P/G6P-P_i part of the diagram may indicate that this reaction pathway favors formation of F6P/G6P under the present conditions.

Chemically, there is no clear route between F6P/G6P and AMP. However, an obvious route exists between F6P and F16BP. The F6P/G6P cluster is negatively correlated with F16BP, implying that the predicted reaction is largely unidirectional; that is, F16BP is formed at the expense of F6P or vice versa. On average, a fluctuation in AMP temporally precedes a response in F16BP and F6P/G6P, but examination of the correlation function reveals that fluctuations in F16BP closely precede (although are nearly contemporaneous with) fluctuations in F6P. Because AMP is positively correlated with F16BP and negatively correlated with F6P/G6P, the prediction of the analysis is that AMP activates the conversion of F6P to F16BP (or that AMP inhibits conversion of F16BP to F6P).

Finally, F16BP is strongly positively correlated with DHAP. The positive correlation implies that if the two are chemically interconverted, then the reaction is most likely near a point of quasi-equilibrium. If chemical conversion of F16BP to DHAP is assumed, then there is a three-carbon fragment we have not measured in this system (this is glyceraldehyde-3-phosphate). Variation in F16BP closely precedes variation in DHAP, implying that DHAP is further, mechanistically, from the inputs than from F16BP.

The pathway as predicted from this analysis (Fig. 5B) can be compared to the network in Fig. 1. Both pathways contain the rapid interconversion of F6P and G6P, interconversion of F6P with F26BP and F16BP, and the rapid interconversion of F16BP with DHAP, all of which form the backbone of the partial glycolytic pathway. Citrate is correctly predicted to effect negatively the conversion of F6P to F26BP, and AMP is correctly predicted to activate the conversion of F6P to F16BP.

The choice of specific connections into the F6P/G6P cluster made by the connection algorithm was not expected. One might expect G6P to be less strongly correlated to AMP and F16BP than is F6P, and there is no particular reason that P_i should be the most highly correlated with G6P. There are a number of reasons why these assignments were made, but the most important is that the high correlation of G6P with F6P makes distinguishing between them statistically nearly impossible. Therefore, relatively small amounts of measurement error in the time series data may lead to reassignment of the connections to F6P and G6P. Inorganic phosphate is most closely associated with the F6P/G6P group because F6P is a product in both reactions that produce the phosphate.

The inhibition of the conversion of F6P to F16BP by citrate (Fig. 1) was not predicted. In our experimental system, this inhibition is not present. Most early studies (*11*, *13*) of the inhibitory effect of citrate on PFK1 were performed in the absence of F26BP. Later studies have shown that F26BP combined with AMP decreases the inhibitory effect of citrate on PFK1 dramatically (*12*, *17*). In our system, we used an excess amount of PFK2 so that we could measure F26BP by CZE. The concentration of F26BP in the system is about five times higher than its physiological level. This high level of F26BP may be responsible for diminishing the inhibition of PFK1 by citrate.

The CMC theory shows a good prediction of the reaction pathway from the measurements in this much-studied biochemical system. Both the MDS diagram itself (Fig. 5A) and the predicted reaction pathway (Fig. 5B) resemble the classically determined reaction pathway (Fig. 1). In addition, CMC measurements yield information about the underlying kinetics of the network. For example, species connected by small numbers of fast reactions will have smaller distances between them than species connected by a slow reaction. We therefore conclude that the CMC method is useful and predict that it will be applicable to many other complex reaction systems.

There are a number of caveats. The predictions about the reaction pathway provide many essentials of the sequence of steps and types of interactions that exist among the measured species of the network, but do not provide all of the details of the chemical mechanism. Furthermore, because not all species in the network were measured, we do not predict the entire pathway but only the part specifically involving the measured species. The fact that the calculation yields a reasonable pathway in the absence of full information is a strength of the analysis. Analyses currently under development are concerned with better estimates of the dependence of variation in one variable on variation in the others and detecting the presence of members of the network that are missing from the time series.

Finally, the interactions predicted by the CMC analysis are always in reference to the reaction conditions, including pH, temperature, and inflow species concentrations. In our experiment, for example, the inhibitory effect of citrate for conversion of F6P to F16BP was missed, probably because of the nonphysiological concentration of F26BP. If we had seeded the reactor with a different concentration of PFK2::F26BPase, although we would not have been able to measure F26BP, we might have seen this interaction.

Even in the face of these difficulties and constraints, CMC provides a powerful method for analyzing multivariate chemical and biochemical time series in order to produce pathway hypotheses and predict likely points of control. Such analyses are becoming increasingly important with the advent of analytical methods for multivariate time-resolved measurements of chemical and biochemical concentrations such as CZE and parallel gene expression monitoring from DNA chips.

REFERENCES AND NOTES

1. A. Arkin and J. Ross, *J. Phys. Chem.* **99**, 970 (1995).
2. L. Stryer, *Biochemistry* (Freeman, New York, ed. 3, 1988).
3. A. Arkin and J. Ross, *Biophys. J.* **67**, 560 (1994).
4. C. G. Hocker, I. R. Epstein, K. Kustin, K. Tornheim, *Biophys. Chem.* **51**, 21 (1994).
5. Solution was flowed into the CSTR through a peristaltic pump at a rate of 0.2 ml/min. A 10,000-MW ultrafiltration membrane (YM 10 Diaflo by Amicon, Beverly, MA) was used to confine the enzymes to the reactor. The solution is stirred with a Teflon stirring disk, which reduced the reactor volume to 1.17 ml.
6. P. J. Oefner, *Electrophoresis* **16**, 46 (1995).
7. Abbreviations for the enzymes: HK, hexokinase; PHI, phosphoglucose isomerase; PFK1, phosphofructokinase 1; F16BPase, fructose-1,6-bisphosphatase; PFK2, phosphofructokinase 2; F26BPase, fructose-2,6-bisphosphatase; TPI, triose-phosphate isomerase; and CK, creatine kinase. Abbreviations for the chemical species in the system: AMP-I, input adenosine monophosphate; citrate-I, input citrate; G6P, glucose-6-phosphate; F6P, fructose-6-phosphate; F16BP, fructose-1,6-bisphosphate; F26BP, fructose-2,6-bisphosphate; DHAP, dihydroxyacetone phosphate; GAP, glyceraldehyde phosphate; P_i, inorganic phosphate; and creatine-P, creatine phosphate.
8. P. Shen, D. Hauri, J. Ross, P. J. Oefner, *J. Capillary Electrophor.* **3**, 155 (1996).
9. All chemicals and enzymes were purchased from Sigma, except for PFK2::F26BPase, which was kindly provided by D. Okar. Reactions were carried out in a solution of 30 mM Hepes, 50 mM potassium chloride, 1.0 mM potassium phosphate, 2 mM dithiothreitol, 5.0 mM magnesium chloride, 0.8 mM adenosine triphosphate (ATP), 2.5 mM creatine-P, and 0.6 mM glucose, buffered at pH 7.1 with sodium hydroxide, which we will refer to as enzyme buffer. All enzymes are from rabbit muscle unless otherwise indicated. The enzymes include HK from baker's yeast; PHI, PFK1, and F16BP from rabbit liver; and aldolase, TPI, CK, and PFK2::F26BPase from rat liver.
10. Chemical separations and quantification were done with an HP ^{3D} Capillary Electrophoresis machine

equipped with photodiode-array detection. The fused silica capillaries used in the experiments were 53 cm in total length (45-cm effective length) with a 50-μm inner diameter and a 320-μm outer diameter. Running conditions were as follows: voltage, −20 kV; current, 17.6 μA; electrolytes, 5.5 mM 4-hydroxybenzoate and 0.5 mM tetradecyltrimethylammonium bromide, pH 11.6.
11. R. G. Kemp, *J. Biol. Chem.* **246**, 245 (1971).
12. E. V. Schaftingen, M. F. Jett, L. Hue, H. G. Hers, *Proc. Natl. Acad. Sci. U.S.A.* **78**, 3483 (1981).
13. G. Colombo, P. W. Tate, A. W. Girotti, R. G. Kemp, *J. Biol. Chem.* **250**, 9404 (1975).
14. E. V. Schaftingen and H. G. Hers, *Biochem. Biophys. Res. Commun.* **101**, 1078 (1981).
15. The enzyme activities were not constant during the entire 12-hour sampling period. Six separate experiments of 2 to 3 hours each were conducted, with the same amount of enzymes (by weight) in each experiment. Nonetheless, the enzyme activities differed slightly between experiments, as indicated by a change in the unperturbed steady-state concentrations of the measured species. In order to make the time series between experiments match, we multiplied the concentrations from the time series in each experiment by the appropriate ratio of the reference concentration (as defined above) to the measured unperturbed steady-state concentration. In order to repeat the last time point of a previous experiment, each experiment repeated the last two to three sets of input from the previous experiment.
16. D. A. Card, D. E. Folmer, S. Sato, S. A. Buzza, J. A. W. Castleman, *J. Phys. Chem.* **101**, 3417 (1997).
17. K. Uyeda, E. Furuya, L. J. Luby, *J. Biol. Chem.* **256**, 8394 (1981).
18. We thank P. Oefner (Department of Biochemistry, Stanford University) for the use of the capillary electrophoresis apparatus and for helpful discussions, and S. Pilkis (deceased) and D. Okar (Department of Biochemistry, University of Minnesota) for providing us with PFK2::F26BPase and for helpful discussions. This work was supported in part by NSF. A.A. was supported in part by Office of Naval Research grant N00014-96-1-0564.

17 April 1997; accepted 7 July 1997

$^{40}Ar/^{39}Ar$ Dating into the Historical Realm: Calibration Against Pliny the Younger

P. R. Renne,* W. D. Sharp, A. L. Deino, G. Orsi, L. Civetta

Laser incremental heating of sanidine from the pumice deposited by the Plinian eruption of Vesuvius in 79 A.D. yielded a $^{40}Ar/^{39}Ar$ isochron age of 1925 ± 94 years ago. Close agreement with the Gregorian calendar–based age of 1918 years ago demonstrates that the $^{40}Ar/^{39}Ar$ method can be reliably extended into the temporal range of recorded history. Excess ^{40}Ar is present in the sanidine in concentrations that would cause significant errors if ignored in dating Holocene samples.

The ability to date geological events in the recent past is increasingly important in many areas of earth science. Applied to volcanogenic materials of high potassium content, the $^{40}Ar/^{40}K$ method of dating has been used to date samples into the Holocene, that is, less than 12,000 years old (*1*), although the precision is lower than is commonly reported for ^{14}C, uranium series, or other methods. The $^{40}Ar/^{39}Ar$ variant of this method, in which ^{40}K is measured by proxy through ^{39}Ar in irradiated samples (*2*), potentially allows recognition of xenocrystic contamination, nonatmospheric initial argon, and argon loss. For example, a young $^{40}Ar/^{39}Ar$ date of 5.3 ± 0.3 thousand years ago (Ka) has been reported (*3*) for sanidine from a tephra derived from the Mono Craters, California, whose age had been previously constrained by ^{14}C at 4.6 ± 0.1 Ka. Determination of this $^{40}Ar/^{39}Ar$ model age relied on the assumption that the significant scatter in apparent ages of single crystals was a result only of xenocrystic contamination.

Dating minerals in volcanic ejecta such as sanidine, which is potassium-rich and is thought to efficiently exclude initial argon at magmatic temperatures, is the most promising approach, although the possible effects of xenocrystic contamination (*4*) can be problematic. Analysis of single crystals, for example by laser fusion, can obviate xenocrystic contamination (*5*), but single crystals are seldom large enough to yield reliably measurable quantities of $^{40}Ar^*$ through radiogenic ingrowth in the Holocene. A relatively large spherical sanidine crystal 2 mm in diameter with 10 weight % K produces only about 2×10^{-18} moles of $^{40}Ar^*$ in 5000 years, and this quantity is one or two orders of magnitude smaller than the best attainable procedural background levels of ^{40}Ar.

We sought to investigate the limits of the $^{40}Ar/^{39}Ar$ method by application to ejecta from the infamous eruption of Vesuvius, which destroyed Pompeii and other Roman cities, as documented in the writings of Pliny the Younger (*6*). Vesuvius erupted pumice clasts up to 36 cm long beginning in the early afternoon of 24 August 79 A.D., 1918 calendar years ago. The white pumice that erupted initially is highly alkaline and contains up to 5% sanidine phenocrysts with 13.7 to 15.7 weight % K_2O (*7*), which are up to 8 mm in diameter. A sample of this pumice was collected at the Villa of Poppea, which was buried in the eruption and has only recently been excavated.

We divided irradiated sanidine from the pumice (*8*) into 12 samples totaling 0.430 g and analyzed them by incremental heating with a CO_2 laser (*9*). The samples yielded imprecise and dispersed apparent ages (*10*) of 24 to 521 Ka in the lower (1 to 2 W) laser power steps, which decreased and became more uniform (2 to 26 Ka) at 4 to 6 W, and became uniformly 2 to 3 Ka in the 7- to 20-W steps. The 1- to 2-W initial steps, each of which contained less than 0.1% of the total ^{39}Ar released, yielded $^{40}Ar/^{36}Ar$ values of 298 to 323, which are statistically indistinguishable at 95% confidence (critical value test) from the atmospheric ratio of 296 (*11*). A table of the argon isotopic data is available to *Science* Online subscribers at www.sciencemag.org.

Cast on an isotope correlation diagram (Fig. 1), the data define an isochron (*12*) that yields an intercept corresponding to $^{40}Ar^*/^{39}Ar_K = 0.07551 \pm 0.0037$, equivalent to an age of 1925 ± 94 years. The initial $^{40}Ar/^{36}Ar$ ratio defined by the isochron is 306.9 ± 1.3, significantly higher than the atmospheric value and indicative of a trapped component of extraneous ^{40}Ar. Excluding the 1- to 2-W steps, which are most likely to contain a significant proportion of adsorbed surficial argon (Fig. 1, inset), the remaining 33 steps yielded an isochron with indistinguishable age (1927 ± 102 years) and initial $^{40}Ar/^{36}Ar$ (306.9 ± 1.5) compared with results from the entire data set. The mean squared weighted deviation (MSWD) values of 0.51 ($N = 46$) and 0.55 ($N = 33$) indicate that observed scatter about the isochron is less than would be expected from the errors in the individual analyses; therefore, the errors on individual analyses are likely to have been slightly overestimated, or some error correlations are unaccounted for in the regression used. Because there is no objective basis for excluding the lowest temperature steps, we prefer the isochron obtained from all 46 analyses as the best estimate of the age of this sample.

The presence of extraneous ^{40}Ar is substantiated by the total gas results; the $^{40}Ar/^{39}Ar$ apparent age (*10*) calculated from the sum of all gas released is 3300 ± 500 years, clearly distinct within error from the known calendar age. With the known age, the con-

P. R. Renne, Berkeley Geochronology Center, 2455 Ridge Road, Berkeley, CA 94709, USA, and Department of Geology and Geophysics, University of California, Berkeley, CA 94720, USA.
W. D. Sharp and A. L. Deino, Berkeley Geochronology Center, 2455 Ridge Road, Berkeley, CA 94709, USA.
G. Orsi, Dipartamento di Geofisica e Vulcanologia, Università di Napoli, Largo Santo Marcellino 10, Napoli, Italy.
L. Civetta, Dipartamento di Geofisica e Vulcanologia Università di Napoli, Largo Santo Marcellino 10, Napoli, Italy, and Vesuvian Volcanological Observatory, 249 Via Manzoni, Napoli, Italy.

*To whom correspondence should be addressed at Berkeley Geochronology Center, 2455 Ridge Road, Berkeley, CA 94709, USA.